Applied Physics Letters

Interface resolved magnetism at metal–organic (Fe/Alq_3) interfaces under x-ray standing wave condition

Cite as: Appl. Phys. Lett. **116**, 101603 (2020); https://doi.org/10.1063/1.5135361
Submitted: 07 November 2019 . Accepted: 27 February 2020 . Published Online: 13 March 2020

Avinash Ganesh Khanderao, Ilya Sergueev, H. C. Wille, and Dileep Kumar

Applied Physics Letters ARTICLE scitation.org/journal/apl

Interface resolved magnetism at metal–organic (Fe/Alq_3) interfaces under x-ray standing wave condition

Cite as: Appl. Phys. Lett. **116**, 101603 (2020); doi: 10.1063/1.5135361
Submitted: 7 November 2019 · Accepted: 27 February 2020 ·
Published Online: 13 March 2020

Avinash Ganesh Khanderao,[1] Ilya Sergueev,[2] H. C. Wille,[2] and Dileep Kumar[1,a)]

AFFILIATIONS

[1]UGC-DAE Consortium for Scientific Research, Indore, India
[2]Deutsches Elektronen-Synchrotron DESY, Notkestraße 85, 22607 Hamburg, Germany

[a)]**Author to whom correspondence should be addressed**: dkumar@csr.res.in

ABSTRACT

The isotope selective grazing-incidence nuclear resonance scattering (GI-NRS) technique, which is a time analog to Mössbauer spectroscopy, is made depth resolved to probe the magnetism of the diffused Fe ($Fe_{diffused}$) and bulk Fe (Fe_{bulk}) parts of the layer in an Fe/Alq_3 [ferromagnetic (FM)/organic semiconductor (OSC)] bilayer structure. On the basis of theoretical simulations, it is demonstrated that the antinode regions of x-ray standing waves (XSWs) generated through wave guide structures allow one to measure the $Fe_{diffused}$ and Fe_{bulk} parts independently, providing evidence for a diffused layer with reduced electron density and hyperfine fields. Due to possible small isolated clusters of Fe in the diffused layer, Fe moments are found with random orientations, while in Fe_{bulk} moments, they are aligned in the film plane due to shape anisotropy. GI-NRS under XSW is suitable for FM/OSC structures to obtain interface resolved magnetic information, which is otherwise difficult with any other available lab based conventional methods.

Organic spintronics is one of the latest and most interesting developments, where organic semiconductors (OSCs) are sandwiched between two ferromagnetic (FM) layers to obtain spin-polarized electron transport.[1,2] A significant amount of effort has been made to understand spin injection, manipulation, and detection in organic spin valves (OSVs) since their discovery.[3,4] Interfaces between layers of FM and organic material play a decisive role in the functionality of OSC devices for spintronics applications. Specifically, the diffusion and penetration of the top electrode are found to play a vigorous role in controlling the performance of such spintronics devices. In extreme cases, the atoms of the top FM layer penetrate deep into the organic layer, making a conductive pathway to the bottom electrode and leading to OSV failure.[5] Over the years, it has been realized that the interfaces in the FM-OSC structure hold the key to develop an understanding about the remarkable properties of the OSV devices. In view of this fact, considerable efforts are being put together to understand the magnetic and structural properties of the diffused layer at the FM-OSC interfaces. However, an efficient spin injection in the OSV device is yet to be experimentally realized.[6] In fact, the study of the top electrode on OSV is still in a priority list for researchers to get a clear understanding of the growth and magnetic behavior of metal in the vicinity of OSC, but it is still difficult to accurately determine the interface magnetism and to correlate the same with OSV magnetic and transport properties unambiguously.

Conventional lab based magnetic characterization techniques, such as the magneto-optical Kerr effect (MOKE),[7] superconducting quantum interface device (SQUID),[8] vibrating sample magnetometer (VSM),[9] Mössbauer spectroscopy with a ^{57}Fe probe layer,[10] and nuclear magnetic resonance (NMR),[11] either do not have enough depth resolution so as to resolve the interfaces or may not be probing the real interfaces. Conversion electron Mössbauer spectroscopy (CEMS),[12] polarized neutron reflectivity (PNR),[13] and x-ray absorption spectroscopy (XAS)[14] are more informative and powerful methods for depth resolved studies. However, each technique has its own advantages and disadvantages, which mainly depend on the type of sample and the nature of magnetic studies. For example, in the case of CEMS, depth selectivity can be achieved with a thin probe resonant layer, embedded at a definite depth.[15,16] For the study of depth dependent magnetism, a set of samples needs to be prepared with a probe resonant layer at different depth positions. However, even in the best deposition methods available, full reproducibility is difficult to achieve in separate depositions. In general, PNR is also not an appropriate technique for FM-OSC interfaces due to the relatively very long

measurement time (several hours) in the case of the deeply diffused FM layer (reduced scatters per unit volume in the interface region). In addition, it usually requires a big sample in order to have sufficient neutron scattering from the interface. Liu *et al.* have studied the Co/Alq_3/Fe spin valve using PNR, where the Co/Alq_3 interface could not be studied due to the limited sensitivity of the PNR to the few tens of angstrom thick Co layer.[17]

On the other hand, the synchrotron radiation based grazing incident nuclear resonant scattering (GI-NRS)[18] technique detects scattered resonant counts from the thin sample. Besides its own limitation of isotope selectivity to the limited materials (^{57}Fe, ^{119}Sn, ^{121}Sb, ^{125}Te, ^{193}Ir, etc.)[19] a high scattering yield of the technique makes it possible to measure even a fraction of a monolayer of isotope material within a reasonable time.[20] In order to enhance interface contribution along with depth sensitivity, the x-ray standing wave (XSW) technique[21] has been used. Here, the x-ray field intensity in the layered structure is confined to specific regions of the thin layers (with a length scale ~0.1–100 nm) using wave guide structures. The generation of XSW is similar to the literature, where x-ray based measurements such as fluorescence,[22] extended x-ray absorption fine structure (EXAFS),[23] and x-ray diffraction (XRD)[24] were made interface selective[25] for their structural or electronic properties. x-ray magnetic circular dichroism (XMCD) measurements under XSW generated through a W/B4C multilayer have been used in the literature to understand the change in Co magnetism near the Co-on-Pd interface.[26] Andreeva *et al.*[27] have investigated depth selectivity of hyperfine fields in a thin iron layer in the Fe/Nb structure by producing XSW using underneath a $[Mo/Si]_{45}$ multilayer. In general, XSW based studies in the literature have not been explored to probe interface magnetism of FM-OSC structures. In the present work, GI-NRS and fluorescence (XRF) are combined with XSW techniques, adding extra dimensions to measure interface resolved magnetism at the Fe–Alq_3 interface. Theoretical results have been shown first to bring out the potential of the GI-NRS under XSW conditions, and then the feasibility of performing such experiments has been demonstrated by probing the depth resolved information of the Fe layer in the Fe/Alq_3 bilayer structure.

X-ray standing waves are generated by making use of the total external reflection from a dense surface. When x-rays are incident below a critical angle (θ_c), it is then totally reflected from a flat reflecting surface. Interference occurs above the mirror surface where the XSW field is formed by the interference between the incident and reflected plane waves. In this case, the electric field intensity (EFI) in the vacuum above the surface is found to be[21]

$$\mathrm{I(q,z)} = \left|E_0^i + E_0^r\right|^2 = I_0\left[1 + \mathrm{R} + 2\sqrt{\mathrm{R}}\cos(\upsilon - 2\pi \mathrm{Qz})\right], \quad (1)$$

where $R = \left|\frac{E_0^r}{E_0^i}\right|^2$ is the reflectivity (expected to close to unity below the critical angle-θ_c), $I_0 = \left|E_0^i\right|^2$ is the incident intensity, E_0^i and E_0^r are the amplitudes of the incident and reflected x-ray wave fields, and Q is the magnitude of the wave vector transfer: $Q = k_R - k_0$. In the case of the planar x-ray wave guide, XSWs are generated by sandwiching a layer of a low-z element between two layers of a high-z element.[28] When x-rays fall at grazing incidence, several transverse electric modes of such a structure can be excited under the condition

$$\phi_n = (n+1)\lambda/2d, \quad (2)$$

where ϕ_n is the angle at which the x-rays fall, and λ, d, and n are the wavelength of x-rays, the thickness of the cavity, and the order of the mode, respectively.

The x-ray reflectivity (XRR) pattern and formation of XSW (variation of EFI) with an increasing incident angle from $q_{in} = 0$ to 0.08 Å^{-1} are simulated using Parratt's recursion algorithm[29] for a planner wave guide structure; Si (substrate)/Pt-400Å ($\rho_1 = 21.45$ g/cm^3)/Alq_3-500Å ($\rho_2 = 1.3$ g/cm^3)/Pt-30Å ($\rho_3 = 21.45$ g/cm^3) by taking an incident x-ray of energy 14.4 keV. Here, a less dense organic semiconductor layer Alq_3 [Tris(8-hydroxyquinolinato) aluminum] works as a cavity for this planner wave guide structure.[30] As clear from the simulated contour plot in Fig. 1(b), resonance enhancement of the x-ray intensity inside the cavity takes place whenever the condition in Eq. (2) is satisfied for the *n*th mode. Well localized antinodes of the x-ray standing waves corresponding to TE0, TE1, TE2, and TE3 modes of the wave guide structure are clearly visible at a fixed value of $q_1 = 0.036$ Å^{-1}, $q_2 = 0.041$ Å^{-1}, $q_3 = 0.048$ Å^{-1}, and $q_4 = 0.058$ Å^{-1}.

In order to establish how such a structure can improve the depth sensitivity, a 160 Å thick Fe marker layer is placed in the Alq_3 cavity and XRR with the EFI distribution again simulated for the sample structure; Si (substrate)/Pt (400 Å)/Alq_3 (440 Å)/Fe (160 Å)/Alq_3 (40 Å)/Pt (30 Å) and plotted in Figs. 2(a) and 2(b). The Fe layer is divided into two parts, viz., 60 Å Fe_{bulk} and 100 Å $Fe_{diffuse}$ and placed such that the antinodes corresponding to TE3 and TE4 modes lie on the diffused and bulk parts of the Fe layer. Fe fluorescence as a function of $q = 4\pi \sin\phi/\lambda$, with ϕ being the angle of incidence, is calculated for following three different electron density (ρ) combinations of Fe_{bulk} and $Fe_{diffused}$ layers as (i) $\rho_{bulk} = 7.874$ g/cm^3 and $\rho_{diffused} = 4.170$ g/cm^3, (ii) $\rho_{bulk} = 5.748$ g/cm^3 and $\rho_{diffused} = 4.170$g/cm^3, and (iii) $\rho_{bulk} = 7.874$ g/cm^3 and $\rho_{diffused} = 6.290$ g/cm^3 as shown in Figs. 2(c-i), 2(c-ii), and 2(c-iii). The calculated Fe–K_α fluorescence spectrum consists of several peaks corresponding to the dips in XRR below the θ_c of Pt as shown in Fig. 2(a).

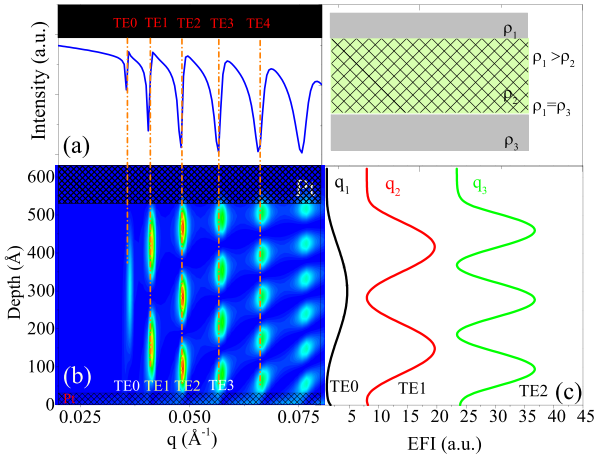

FIG. 1. (a) XRR shows the TE0, TE1, TE2, and TE3 XSW modes formed inside the Alq_3 layer (b) calculated EFI distribution as a function of depth and scattering vector inside the planar wave guide structure: Si/Pt(400 Å)/Alq_3 (500 Å)/Pt (30 Å) and the corresponding simulation. (c) EFI variation along the depth at $q_1 = 0.036$ Å^{-1}, $q_2 = 0.041$ Å^{-1}, and $q_3 = 0.048$ Å^{-1}; plots are shifted vertically for the sake of clarity.

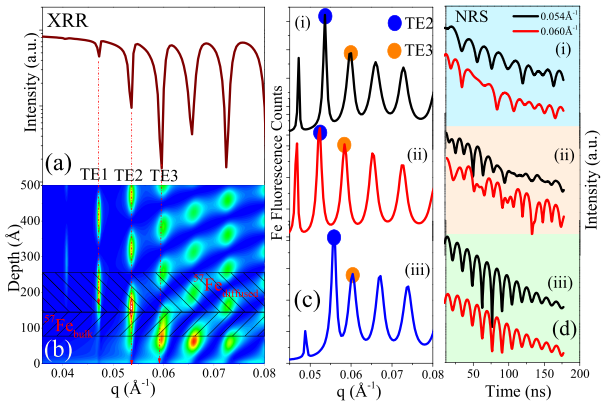

FIG. 2. (a) Represents the simulated XRR for Si/Pt/Alq_3/Fe(diffused)/Fe(bulk)Alq_3/Pt as a function of q. (b) Simulated contour plot for the Si/Pt/Alq_3/Fe (diffused)/Fe(bulk)/Alq_3/Pt. The XSW modes are clearly visible inside the wave guide structure. The shaded region represents the bulk and diffused Fe layers. (c) Simulated XRF for varying electronic parameters for (i) $\rho_{bulk} = 7.874$ g/cm^3 and $\rho_{diffused} = 4.170$ g/cm^3, (ii) $\rho_{bulk} = 5.748$ g/cm^3 and $\rho_{diffused} = 4.170$ g/cm^3, and (iii) $\rho_{bulk} = 7.874$ g/cm^3 and $\rho_{diffused} = 6.290$ g/cm^3. (d) Simulated NFS spectra for the same electron densities of diffused and bulk Fe layer with (i) different hyperfine fields and the same spin orientations of the bulk and diffused layer, (ii) different moment orientation and the same hyperfine field of the bulk and diffused layer, and (iii) different hyperfine field and the same spin orientations without the XSW condition.

It may be noted that the fluorescence at any given value of q is found by integrating the concentration profile $\rho(z)$ of the Fe layer weighted with the x-ray intensity I(q, z) at that depth,[25]

$$T(q) \propto \int I(q,z)\rho(z)dz. \tag{3}$$

$I(q,z)$ is obtained as the square of the magnitude of the total field $\left|E_0^i + E_0^r\right|^2$ as given in Eq. (1). The origin of the Fe–K_α fluorescence peaks in Fig. 2(c) can be understood with the help of the simulated EFI shown in Fig. 2(b).

For $q_1 \approx 0.054$ Å^{-1}, the rth antinode overlays with the $Fe_{diffused}$ layer, giving rise to the peak in the fluorescence at ~0.054 Å^{-1}. However, as the q is increased further, (r + 1)th antinode partially overlaps with the Fe_{bulk} layer at $q_2 \approx 0.060$ Å^{-1} and gives rise to the related peak in fluorescence. The shape and intensity of the second peak mainly depend upon the concentration variation in the $Fe_{difussed}$ layer, while the shape of the third peak depends upon the Fe concentration profile across the Fe_{bulk} layer. In view of the fact, the fluorescence intensities of the second and third peaks are very sensitive to the subtle change in the concentration, thickness, and roughness of Fe_{bulk} and $Fe_{diffused}$ layers. Even a small variation in the depth and electron density of either part of the Fe layer would result in a significant variation in the relative intensities of fluorescence peaks corresponding to TE3 and TE4 modes. It is clear that the Fe-K_α fluorescence peaks as pointed in Fig. 2(c) correspond preferentially to the Fe_{bulk} and $Fe_{diffused}$ layers.

GI-NRS is a time analog to Mossbauer spectroscopy and sensitive to hyperfine field and spin orientations of the resonant isotope (^{57}Fe) layer (one of the Mossbauer isotopes).[31] The scattering amplitude from a resonant ^{57}Fe layer is given by[15]

$$r(\omega) = i\frac{\lambda}{\sin\theta}\cdot\sigma\cdot\left[f^{el}+f^{nucl}(\omega)\right], \tag{4}$$

where λ is the wavelength of the resonant radiation (For ^{57}Fe, $\lambda = 0.8604$ Å), θ is the incident angle, σ is the surface density of the scattering centers, and f^{el} and f^{nucl} are non-resonant and resonant scattering amplitudes. As nuclear excitation decays slowly as compared to the electronic scattering (prompt), therefore nuclear resonance response is measured after time gating of the electron scattering part. The electronic contribution to the non-resonant scattering has only a weak dependence on the x-ray energy, whereas nuclear resonance depends upon the nuclear transition energies. Therefore, the nuclear resonant scattering amplitude exhibits a variation with the hyperfine field and the spin orientations in the form of quantum beats in the NRS pattern and hence is useful in the determination of magnetic hyperfine structure along with the direction of the magnetization in thin films. The technical details of the NRS method can be found in Ref. 27. It may be noted that, as compared to the square dependence influence on secondary radiation such as x-ray fluorescence, the intensity of the nuclear resonance part from the thin layer is proportional to the fourth power of the standing wave amplitude and hence has more sensitivity compared to the XSW based conventional techniques.[32]

Figure 2(d) shows the GI-NRS delay spectrum calculated using REFTIM[33] software at $q_1 = 0.054$ Å^{-1} and $q_2 = 0.060$ Å^{-1} by assuming (i) different magnitudes of the hyperfine field of $^{57}Fe_{bulk} \sim 33$ T and $^{57}Fe_{diffused} \sim 20$ T and (ii) the same hyperfine field (33 T) in both layers but with different spin orientations as shown in Figs. 2(d-i) and 2(d-ii), respectively. In order to further confirm the noteworthy role of XSW, the same calculation was repeated for identical sample structures just by removing the wave guide structure by eliminating the top and bottom Pt layers from the sample for the simulation as shown in Fig. 2(d-iii). It should be noted that in comparison to Figs. 2(d-i) and 2(d-ii), no significant changes in the GI-NRS beat patterns are observed in Fig. 2(d-iii), which clearly demonstrates the capability of XSW based GI-NRS measurements, where diffused and bulk parts of ^{57}Fe can be resolved in the single sample just by changing the incident angles.

In order to demonstrate the applicability of the XSW based method for depth resolved studies in the experiments, wave guide structure Si/Pt (400 Å)/Alq_3 (500 Å)/^{57}Fe (120 Å)/Ag (20 Å) was deposited under vacuum conditions. The organic layer Alq_3 was sublimated from the commercial source (sublimated grade, >99% pure, supplied by Sigma Aldrich) at a constant rate of 0.02 nm s^{-1}. The ^{57}Fe and Ag layer are deposited on an Si/Pt (400 Å) template using electron beam evaporation in ultra-high vacuum (UHV). An Ag layer is used to complete the wave guide structure and to prevent the Fe layer from oxidation during the *ex situ* experiments. The GI-NRS (delayed) and XRR (prompt) measurements were carried out at the nuclear resonance beam line (P01) at PETRA III, Germany using a photon beam energy of 14.41 keV to excite the ^{57}Fe nuclei in the sample.[34] During measurements, the synchrotron was operated in the 40 bunch mode with a bunch separation of 192 ns. The detector used in the experiment was an avalanche photodiode, which has a time resolution of ~1 ns. Figure 3(a) gives the XRR of the wave guide structure, where sharp dips observed in the reflectivity below the critical angle of Pt, indicate the resonance coupling of incident x-rays to the wave guide, corresponding to the different XSW modes. The XRR is fitted using Parratt's formulism to obtain the thickness and density depth profiling

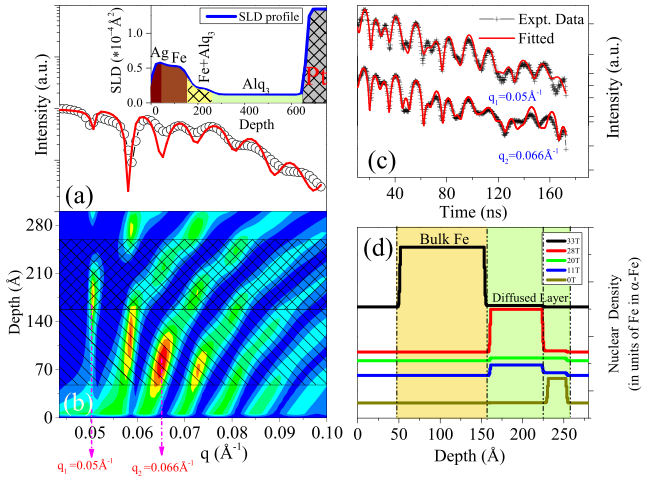

FIG. 3. (a) Represents the x-ray reflectivity of substrate/$Pt^{400Å}$/$Alq_3^{500Å}$/$Fe^{150Å}$/$Ag^{50Å}$ as a function of scattering vector q. The red continuous curves represent the best fit to the data. The scattering length electron density profile (SLD) profile for the fitted structure is shown in the inset. The critical angle of Pt is denoted by θ_c. (b) The contour plot of the x-ray field inside the wave guide structure as a function of depth and scattering vector *q*. Here, the antinodes are at $q_1 = 0.05\,Å^{-1}$ and $q_2 = 0.066\,Å^{-1}$. (c) Represents the nuclear forward scattering time spectra for the Si/Pt/Alq_3/Fe/Ag structure at q_1 and q_2 corresponding to the diffused and bulk layers of Fe, respectively. (d) The distribution of the hyperfine field along with depth. The graphs are vertically shifted for clarity.

of the sample structure. The inset of Fig. 3(a) shows the scattering length electron density profile (SLD) along the depth of the sample. In order to best fit the experimental data, the Fe layer was divided into diffused layers having reduced electronic densities. The 2D contour plot for the wave guide structure is shown in Fig. 3(b); the bulk and diffused layer are marked in the plot. It is clear from the contour plot that the bulk and diffused parts coincide with antinodes at $q_a = 0.050\,Å^{-1}$ and $q_b = 0.066\,Å^{-1}$. As discussed before, measurements performed at these q_a and q_b will provide us information on the diffused and bulk layer. GI-NRS measurements, as shown in Fig. 3(c), were performed at grazing angles $q_a = 0.050\,Å^{-1}$ and $q_b = 0.066\,Å^{-1}$. The quantum beat pattern at different q values, which originates from the interference of the different hyperfine components, is significantly different due to a possible interfacial layer with a reduced hyperfine field and spin orientation.

The quantitative magnetic information along with structural information were obtained by fitting GI-NRS and XRR data simultaneously using the REFTIM software.[33] Here, XRR fixed the structural part of the whole sample structure, whereas GI-NRS helped in modeling magnetic and spin alignment in the Fe layer. Although the GI-NRS fitting has been initiated with roughly estimated hyperfine field values, but the final values have been obtained by taking different combinations of the hyperfine field in different parts (one bulk and two diffused layers) of the Fe layer, which fitted GI-NRS data well with least squares fitting. The hyperfine field of 33T corresponds to the bulk Fe whereas, the diffused layer contains a reduced hyperfine field of 28T, 20T, 11T, and 0T. The variation of various hyperfine fields as a function of depth is shown in Fig. 3(d). This reduced hyperfine field in the diffused part is due to the change in the chemical environment near the Fe and possible size dependent paramagnetism at the buried part. Fe atoms diffuse deep into the Alq_3 layer (>100 Å) due to the soft nature of the Alq_3 film. Due to higher surface tension of the metals compared to organic layers, the metal atom tries to organize into clusters[35] in order to minimize their surface/interface energy.[36] The formation of metal clusters, when deposited on polymers, has already been studied in detail in the literature.[37] In such systems, metal clustering takes place even at a considerable distance below the interface,[38] similar to the present study. The contribution of the ferro-magnetically inactive layer (a negligible hyperfine field at a deep interface) is mainly due to some amount of Fe clusters which are still very small (paramagnetic in nature) which do not contribute to the magnetism of the Fe layer.

In conclusion, on the basis of theoretical understanding through simulation, it is demonstrated that the XSW based GI-NRS technique is capable of providing independent magnetic properties of the diffused and bulk parts of the FM layer in an FM/organic semiconductor (OSC) bilayer structure. An enhanced NRS signal from the buried diffused layer was achieved using localization of the x-ray field inside the wave guide structure, which allows one to measure both parts of the FM layers independently in the same sample, providing evidence of the enhanced capability of the GI-NRS technique under the XSW condition. The feasibility of the experiments has also been demonstrated by depositing the Fe/Alq_3 bilayer structure in the XSW wave guide. The present combined experiments provide evidence of Fe layer diffusion in Alq_3 films with reduced electron density and hyperfine fields. Due to possible small isolated clusters of Fe in the diffused layer, Fe moments are found with random orientation, while in Fe, bulk moments are aligned on the film plane due to shape anisotropy. The present work revealed that GI-NRS under XSW is suitable for magnetic depth profiling of FM/OSC systems, where the FM atom diffuses deep into the soft OSC layer and is sometimes responsible for the OSV device failure.

Portions of this research were carried out at the light source PETRA III of DESY, a member of Helmholtz Association (HGF). We would like to thank Olaf Leupold and Réne Steinbruegge for the assistance at beamline P01, PETRA III. Financial support from the Department of Science and Technology (Government of India) (Proposal No. I-20180885) provided within the framework of the India@DESY collaboration is gratefully acknowledged.

REFERENCES

[1]G. Szulczewski, S. Sanvito, and M. Coey, Nat. Mater. **8**, 693–695 (2009).
[2]M. Gobbia and E. Orgiu, J. Mater. Chem. C **5**, 5572–5580 (2017).
[3]C. Rolin, E. Kang, J.-H. Lee, G. Borghs, P. Heremans, and J. Genoe, Nat. Commun. **8**, 14975 (2017).
[4]Z. G. Yu, Phys. Rev. Lett. **111**, 016601 (2013).
[5]R. Geng, H. M. Luong Timothy, T. Daugherty, and L. Hornak, "Tho Duc Nguyen," J. Sci.: Adv. Mater. Devices **1**(3), 256–272 (2016).
[6]J. Devkota, R. Geng, R. Chandra Subedi, and T. D. Nguyen, Adv. Funct. Mater. **26**(22), 3881–3898 (2016).
[7]D. Kumar, A. Gupta, P. Patidar, A. Banerjee, K. K. Pandey, T. Sant, and S. M. Sharma, J. Phys. D: Appl. Phys. **47**(10), 105002 (2014).
[8]G. Tsoy, Z. Janu, M. Novak, F. Soukup, and R. Tichy, Phys. B: Condens. Matter **284–288**, 2122–2123 (2000).
[9]A. W. Pacyna and K. Ruebenbauer, J. Phys. E **17**, 141 (1984).
[10]L. K. Perry, D. H. Ryan, and R. Gagnon, Hyperfine Interact. **170**, 131–143 (2007).
[11]W. Soonho, S. Seung-Bo, L. Soonchil, L. Sanggap, K. Kiwoong, and H. Yunseok, Sci. Rep. **3**, 3189 (2013).

[12]R. Gellert, O. Geiss, G. Klingelhöfer, H. Ladstätter, B. Stahl, G. Walter, and E. Kankeleit, Nucl. Instrum. Methods Phys. Res., Sect. B **76**, 381–382 (1993).
[13]S. Couet, K. Schlage, T. Diederich, R. Rüffer, K. Theis-Bröhl, B. P. Toperverg, K. Zhernenkov, H. Zabel, and R. Röhlsberger, New J. Phys. **11**, 013038 (2009).
[14]Y. Kayser, J. Sá, and J. Szlachetko, Anal. Chem. **87**(21), 10815–10821 (2015).
[15]M. A. Andreeva and B. Lindgren, Phys. Rev. B **72**, 125422 (2005).
[16]L. Niesen, A. Mugarza, M. F. Rosu, R. Coehoorn, R. M. Jungblut, F. Roozeboom, A. Q. R. Baron, A. I. Chumakov, and R. Rüffer, Phys. Rev. B **58**, 8590 (1998).
[17]Y. Liu, S. M. Watson, T. Lee, J. M. Gorham, H. E. Katz, J. A. Borchers, H. D. Fairbrother, and D. H. Reich, Phys. Rev. B **79**, 075312 (2009).
[18]K. Schlage and R. Röhlsberger, J. Electron Spectrosc. Related Phenom. **189**, 187–195 (2013).
[19]P. Alexeev, O. Leupold, I. Sergueev, M. Herlitschke, D. F. McMorrow, R. S. Perry, E. C. Hunter, R. Röhlsberger, and H.-C. Wille, Sci. Rep. **9**, 5097 (2019).
[20]W. A. A. Macedo, B. Sahoo, J. Eisenmenger, M. D. Martins, W. Keune, V. Kuncser, R. Röhlsberger, O. Leupold, R. Rüffer, J. Nogués, K. Liu, K. Schlage, and I. K. Schuller, Phys. Rev. B **78**, 224401 (2008).
[21]M. J. Bedzyk and L. Cheng, Rev. Mineral. Geochem. **49**(1), 221–266 (2002).
[22]G. Das, A. Khooha, A. K. Singh, A. K. Srivastava, and M. K. Tiwari, Appl. Phys. Lett. **108**, 263109 (2016).
[23]J. C. Woicik, T. Kendelewicz, K. E. Miyano, P. L. Cowan, M. Richter, B. A. Karlin, C. E. Bouldin, P. Pianetta, and W. E. Spicer, J. Vac. Sci. Technol., A **10**, 2041 (1992).
[24]D. P. Woodruff, Prog. Surf. Sci. **57**(1), 1–60 (1998).
[25]A. Gupta, D. Kumar, and C. Meneghini, Phys. Rev. B **75**, 064424 (2007).
[26]S.-K. Kim and J. B. Kortright, Phys. Rev. Lett. **86**, 1347 (2001).
[27]M. A. Andreeva, N. G. Monina, L. Häggström, B. Lindgren, B. Kalska, S. Kamali-M, S. N. Vdovichev, N. N. Salashchenko, V. G. Semenov, O. Leupold, and R. Rüffer, Nucl. Instrum. Methods Phys. Res., Sect. B **266**, 187–196 (2008).
[28]A. Gupta, Hyperfine Interact. **160**, 123 (2005).
[29]L. G. Parratt, Phys. Rev. **95**, 359 (1954).
[30]A. Gupta, P. Rajput, A. Saraiya, V. R. Reddy, M. Gupta, S. Bernstorff, and H. Amenitsch, Phys. Rev. B **72**, 075436 (2005).
[31]D. E. Johnson, D. P. Siddons, J. Z. Larese, and J. B. Hastings, Phys. Rev. B **51**, 7909 (1995).
[32]M. A. Andreeva, R. A. Baulina, and Y. L. Repchenko, J. Synchrotron Rad. **26**, 483–496 (2019).
[33]M. A. Andreeva, Hyperfine Interact. **185**(1–3), 17–21 (2008).
[34]H. C. Wille, H. Franz, R. Röhlsberger, W. A. Caliebe, and F. U. Dill, J. Phys.: Conf. Ser. **217**, 012008 (2010).
[35]M. Schwartzkopf and S. Roth, Nanomaterials **6**(12), 239 (2016).
[36]T. L. Morkved, P. Wiltzius, H. M. Jaeger, D. G. Grier, and T. A. Witten, Appl. Phys. Lett. **64**(4), 422–424 (1994).
[37]S. Pletincx, L. L. I. Fockaert, J. M. C. Mol, T. Hauffman, and H. Terryn, Npj Mater. Degrad. **3**, 23 (2019).
[38]F. K. Le Goues, B. D. Silverman, and P. S. Ho, J. Vac. Sci. Technol., A **6**, 2200 (1988).